RSC Advances

PAPER

View Article Online
View Journal | View Issue

Cite this: *RSC Adv.*, 2025, **15**, 36769

Efficient oxidation of hindered amines to nitroxide radicals with hydrogen peroxide over layered double hydroxide

Yupeng Zhang,[a] Wensheng Xu,[a] Zefan Liu,[a] Ligong Chen,[ab] Xilong Yan,[a] Bowei Wang *[ab] and Yang Li *[a]

Alkoxylation of hindered amine light stabilisers is a common strategy to reduce their basicity and expand their application scope. However, the current catalysts used for preparing the nitroxide radical intermediates are limited by their separation and recycling properties. To address this issue, this study proposes a method for the preparation of hindered amine nitroxide radical intermediates using hydrogen peroxide as the oxidant and layered double hydroxides (LDHs) as heterogeneous catalysts. Excitingly, when using only 5.00 wt% LDHs with a Mg/Al ratio of 3 : 1, both the conversion of the hindered amine and the selectivity towards the corresponding nitroxide radical exceeded 99.9%. Moreover, the catalyst was recyclable and could be reused for more than five cycles without significant loss of its activity. Theoretical calculations and radical trapping experiments revealed that LDHs act as solid bases to promote the decomposition of hydrogen peroxide into reactive oxygen species (ROS), thereby synergistically oxidizing hindered amines to nitroxide radical intermediates. The key influencing factors for the catalytic performance were found to be the types and proportions of metal ions in the LDHs. This study has provided a new pathway for the oxidation of hindered amines to the corresponding nitroxide radicals.

Received 14th August 2025
Accepted 19th September 2025

DOI: 10.1039/d5ra05993c

rsc.li/rsc-advances

1 Introduction

Hindered amines (HA) have become highly efficient light stabilisers due to their efficient free radical capture and regeneration mechanisms.[1] However, the strong alkalinity of the hindered piperidine limits its application with acidic materials or acidic additives. To improve the compatibility of HA, low basicity and high compatibility have been achieved by alkoxylation of HA.[2] However, the nitroxide radicalisation of HA is a key step for the alkoxylation of HA. Currently, Na_2WO_4 is the most commonly used catalyst for the oxidation of HA to nitroxide radical intermediates, offering relatively high substrate conversion. However, given the characteristics of its homogeneous catalyst, it suffers from poor recoverability and limited reusability. In contrast, $Mg(OH)_2$, as a heterogeneous catalyst, has also been explored in recent years.[3,4] Nevertheless, it generally exhibits low substrate conversion and poor product selectivity, and its recovery from the final product remains challenging. From homogeneous catalysis with Na_2WO_4 to the application of heterogeneous catalysts such as $Mg(OH)_2$, the development of catalysts for the nitroxylation of HA has consistently progressed towards highly efficient and recyclable heterogeneous systems. Therefore, there is an urgent need for a novel heterogeneous catalyst that not only efficiently activates hydrogen peroxide but also possesses excellent stability and good recyclability.

Layered double hydroxides (LDHs), also known as hydrotalcites, and their calcined products – layered double oxides (LDOs), have attracted intensive attention in recent years due to their wide applications in environmental remediation,[5,6] biomedicine,[7,8] heterogeneous catalysis,[9,10] and photocatalysis.[11–13] In advanced oxidation processes (AOPs) for wastewater treatment, LDHs are commonly used to catalyse hydrogen peroxide to generate reactive oxygen species (ROS) for degradation of organic pollutants.[14,15] These ROS are precisely what are needed to convert HA into nitroxide radicals.[16] Furthermore, the types and compositions of metal ions within the layered hydrotalcites and the interlayer anions can be adjusted, which is conducive to the optimization of the performance of layered hydroxides. Furthermore, the tunability of the metal ion composition in the brucite-like layers and the interlayer anions enables LDHs with excellent modifiability.[17] As heterogeneous catalysts, they offer ease of separation and recyclability.[18] Therefore, the use of LDHs as heterogeneous catalysts for the H_2O_2-driven oxidation of HA to generate hindered amine nitroxide radicals is highly promising.

Therefore, a series of carbonate-intercalated LDH catalysts with diverse metal ions were synthesised and employed to

[a]School of Chemical Engineering and Technology, Tianjin University, Tianjin 300350, P.R. China. E-mail: bwwang@tju.edu.cn; liyang777@tju.edu.cn
[b]Zhejiang Institute of Tianjin University, Shaoxing 312300, P.R. China

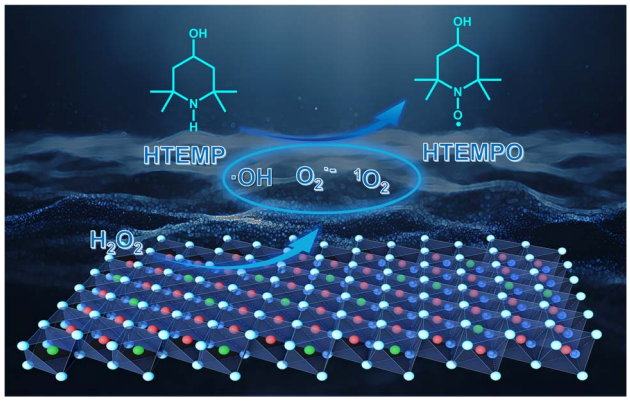

Fig. 1 Generation of reactive oxygen species from hydrogen peroxide catalysed by LDHs for the oxidation of HA to nitroxide radical of HA.

catalyse the oxidation of 4-hydroxy-2,2,6,6-tetramethylpiperidine (HTEMP) to 4-hydroxy-2,2,6,6-tetramethylpiperidine-1-oxyl (HTEMPO) by hydrogen peroxide. Using 5.00 wt% Mg–Al layered double hydroxide (MgAl-LDH, with a Mg/Al ratio of 3 : 1) as the catalyst, HTMEP was efficiently oxidised by hydrogen peroxide to its corresponding nitroxide radical. Both the conversion of HTMEP and the selectivity of HTMEPO exceeded 99.9%. Furthermore, the influence of the types and contents of metal ions in LDHs on the catalytic performance of LDHs was also investigated. The catalytic mechanism and reaction pathway were explored by trapping and quenching ROS involved in the reaction. The reaction pathway was proposed and illustrated in Fig. 1.

2 Experiments

2.1 Materials and methods

$Mg(NO_3)_2 \cdot 6H_2O$ (AR), $Al(NO_3)_3 \cdot 9H_2O$ (AR), $Cu(NO_3)_2 \cdot 3H_2O$ (AR), $Fe(NO_3)_3 \cdot 9H_2O$ (AR), $Ni(NO_3)_2 \cdot 6H_2O$ (AR), $Co(NO_3)_2 \cdot 6H_2O$ (AR), $Zn(NO_3)_2 \cdot 6H_2O$ (AR), Na_2CO_3 (AR), MeOH (AR), EtOH (AR), CH_2Cl_2 (DCM,AR), and deionised water were all purchased from Tianjin Damao Chemical Reagent Factory. NaOH (AR) was supplied by Tianjin Chemical Reagent Plant No. 6. 4-Hydroxy-2,2,6,6-tetramethylpiperidine (98%), coumarin-3-carboxylic acid (98%), sodium tungstate (99%) and nitro blue tetrazolium chloride (NBT, IND) were obtained from Tianjin Heowns Biochemical Technology Co., Ltd. 1,4-Diphenyl-1,3-butadiene (DPBF, 97%) was purchased from Shanghai Dibai Chemical Co., Ltd. *p*-Benzoquinone (*p*-BQ, 99%) and β-carotene (97%) were obtained from Shanghai Macklin Biochemical Co., Ltd. The hindered amine stabiliser SEED (*N*,*N*′-bis(2,2,6,6-tetramethyl-4-piperidyl)-1,3-benzenedicarboxamide, 99%) was purchased from Jiangsu Xinluda Polymer Materials Co., Ltd. Hydrogen peroxide aqueous solution (30%, GR) was obtained from Aladdin Reagent Co., Ltd, Shanghai.

2.1.1 Preparation of Mg–Al hydrotalcite (MgAl-LDH). $Mg(NO_3)_2 \cdot 6H_2O$ (3.85 g, 15.0 mmol) and $Al(NO_3)_3 \cdot 9H_2O$ (1.88 g, 5.00 mmol) were dissolved in 25.0 mL water to afford solution A. NaOH (3.60 g, 90.0 mmol) and Na_2CO_3 (1.06 g, 10.0 mmol) were dissolved in 25.0 mL water to yield solution B. Solutions A and B were simultaneously added dropwise to a four-necked round-bottom flask containing 25.0 mL of water at 25.0 °C under stirring. During the co-precipitation process, the pH of the reaction mixture was maintained between 11 and 12 by the addition rate of solution B. The resulting slurry was aged at 80.0 °C for 8.00 hours. The precipitate was collected by filtration, thoroughly washed with water, and dried at 80.0 °C for 24.0 hours to afford the MgAl-LDH with a molar ratio of 3 : 1. A series of LDHs with a divalent-to-trivalent cation ratio of 3 : 1 were similarly synthesised, including NiAl, CuAl, and ZnAl.

CoAl, MgFe, NiFe, CuFe, ZnFe, and CoFe LDHs were synthesised under the same conditions as above (the corresponding experimental details are described in Section 8 of the SI).

2.2 Characterisation methods

The characteristic structure of synthesised LDHs was identified by X-ray diffraction (XRD, PANalytical B.V. XPERTPRO). Fourier transform infrared spectroscopy (FTIR, FEI USA, Inc. iS50) was employed to analyse the characteristic absorption bands of hydroxyl groups and interlayer anions. The microstructure and morphology of the LDHs were observed using field emission scanning electron microscopy (FE-SEM, FEI Czechoslovakia, Inc. Apreo S). UV-vis spectrophotometry (UV-vis LINESA L8) was employed to monitor the generation of reactive oxygen species in real time during the reaction process. Gas chromatography (GC, Agilent Inc. USA. SP-7890 PLUS) equipped with an Agilent DB-17 capillary column was used to determine the reaction conversion and selectivity. Electron paramagnetic resonance spectroscopy (EPR, Bruker, Germany EMX plus), with 5,5-dimethyl-1-pyrroline *N*-oxide (DMPO) as the spin-trapping agent, was applied to detect reactive oxygen species in the reaction system. Thermogravimetric analysis (TGA, NETZSCH, Germany) was performed to record the thermal decomposition behaviour of the LDHs. CO_2 temperature-programmed desorption (CO_2-TPD, Microtrac BELCat II) was used to evaluate the alkaline strength and quantity of LDHs. X-ray photoelectron spectroscopy (XPS, Thermo Fisher) was conducted to collect survey spectra and high-resolution O 1s spectra.

2.3 Experimental protocol

2.3.1 Nitrogen–oxygen radicalisation reaction. HTEMP (1.57 g, 0.0100 mol) and 15.0 mL water were added to a 100 mL round-bottomed flask. Subsequently, a specified amount of LDHs and 30.0% aqueous hydrogen peroxide solution were added to the reaction vessel. The mixture was stirred at 60.0 °C for 8.00 hours. The conversion and selectivity were determined by GC. Five reaction cycles were carried out under optimized conditions to evaluate the cycle application performance of the optimal catalyst.

2.3.2 Nitroxyl radicalisation of the hindered amine light stabiliser SEED. SEED (1.00 g, 2.25 mmol), MgAl-LDH (50.0 mg, 5.00 wt%) and 15.0 mL ethanol were added to a 50 mL round-bottom flask. Subsequently, 30.0% aqueous hydrogen peroxide (4.09 mL, 36.1 mmol) was added, and the mixture was stirred at 60.0 °C for 8.00 hours.

In a parallel experiment, SEED (1.00 g, 2.25 mmol), Na_2WO_4 (50.0 mg, 5.00 wt%), and 15.0 mL of ethanol were introduced into another 50 mL round-bottom flask, followed by the addition of 30.0% H_2O_2 solution (4.09 mL, 36.1 mmol). The reaction was also conducted at 60.0 °C for 8.00 hours.

2.4 Density functional theory (DFT) calculation

All density functional theory (DFT) calculations were conducted using Gaussian16 software package, Revision C.01.[19] Geometry optimizations and single point calculations of all molecules were performed with the M06-2X functional[20] and the def2-TZVP basis set.[21] The vibrational frequencies of all species were calculated at the same level and it was ensured that all structures are stable.

3 Results

3.1 Preparation and characterisation of LDHs

A series of LDHs catalysts were prepared by co-precipitation followed by hydrothermal treatment, which were classified as Al-based or Fe-based catalysts according to the trivalent metal ions incorporated. The XRD pattern of the MgAl-LDH catalyst (Fig. 2) displayed a characteristic (003) diffraction peak at 11°, along with a doublet peaks near 60° corresponding to the (110) and (113) faces, confirming the successful synthesis of LDHs.[22–26] For LDHs synthesised with different metal ions, the presence of the Jahn–Teller effect in certain ions induces lattice distortion through stretching and compression of the layers. As a result, the characteristic (003) diffraction peak of these LDHs exhibits varying degrees of shift and changes in full width at half maximum (FWHM). To further confirm that the incorporated Jahn–Teller-active metal ions influence the XRD patterns of the synthesised LDHs, we performed SEM characterisation.[27] The image of SEM (Fig. S1) revealed that MgAl-LDH exhibited a relatively smooth and regular surface, indicating no significant Jahn–Teller distortion. In contrast, NiAl-LDH showed evident agglomeration attributed to compressive-type distortion, while CuAl-LDH displayed a transformation of grains into rod-like structures, consistent with elongation-type distortion. ZnAl-LDH, similar to MgAl-LDH, exhibited a smooth and uniform morphology, suggesting the absence of a pronounced Jahn–Teller effect. These observations were in good agreement with the corresponding XRD results. SEM images of the other LDHs shown in Fig. S1 exhibited the morphologies consistent with their respective Jahn–Teller distortions and XRD pattern variations. Energy-dispersive X-ray spectroscopy (EDS) elemental mapping was also performed on the synthesised catalysts (Fig. S2), confirming that the elemental distribution was uniform and consistent with the initial 3 : 1 molar ratio of divalent to trivalent metal ions.

The synthesised catalysts were characterised by FTIR (Fig. 2). Both Al and Fe-based catalysts exhibited a broad absorption band around 3480 cm^{-1} corresponding to surface hydroxyl groups,[28] and a characteristic band near 1360 cm^{-1} attributed to interlayer carbonate anions.[29–34] Additionally, metal–oxygen (M–O) vibrations associated with the hydroxide layers were observed in the fingerprint region,[35] confirming the successful synthesis of various types of hydrotalcites. Therefore, XRD and FTIR characterisations confirmed the successful formation of

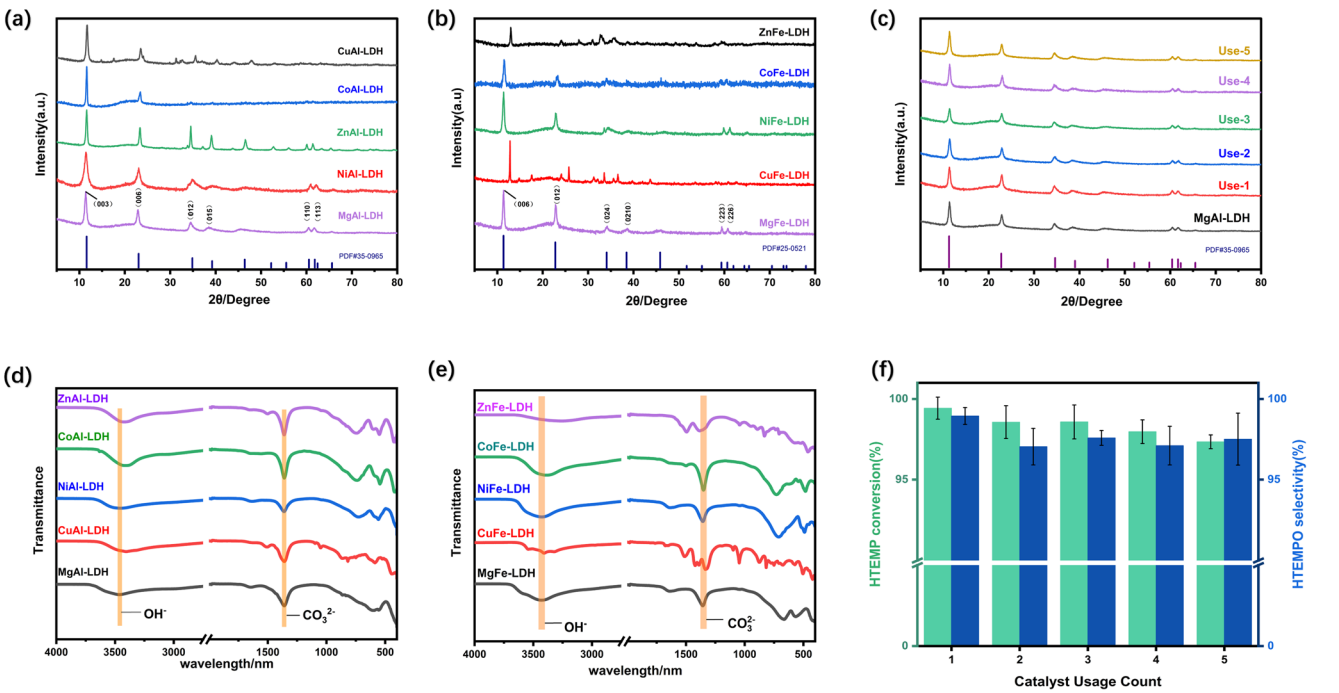

Fig. 2 (a) XRD patterns of Al-based hydrotalcites (b) XRD patterns of Fe-based hydrotalcites (c) the XRD patterns of the recycling catalyst for each run (d) FTIR spectra of Al-based hydrotalcites (e) FTIR spectra of Fe-based hydrotalcites (f) the conversion and selectivity of each run of the five reaction cycles with recycling catalyst.

the layered structure of the LDHs and the intercalation of carbonate anions between the layers.

3.2 Optimisation of nitroxide radicalisation conditions and reusability of catalyst

3.2.1 Optimal reaction conditions for hindered amine *N*-oxidation. The reaction was monitored by GC, and the reaction conditions was optimized upon the criteria shown in SI. The results indicated that the highest conversion of HTEMP and selectivity toward HTEMPO were achieved using 5.00 wt% MgAl-LDH and 8.00 equivalents of hydrogen peroxide at 60.0 °C for 8.00 hours. In contrast, LDHs containing Fe^{3+}, Cu^{2+}, or Co^{2+} exhibited poor catalytic performance, likely due to their strong catalytic activity on the decomposition of hydrogen peroxide into oxygen, leading to a significant loss of the oxidant.[36,37]

3.2.2 Reusability of the catalyst. To verify the stability of MgAl-LDH, five consecutive catalytic cycles were conducted using the optimised catalyst dosage identified in the screening experiments. The results are presented in Fig. 2f. Additionally, the catalyst after each cycle was characterised by powder X-ray diffraction (Fig. 2c).

After five reaction cycles, the conversion and selectivity of the reaction were maintained with this catalyst. The XRD results confirmed that the lamellar structure of the hydrotalcite remained intact without any collapse or significant changes, demonstrating the excellent stability and reusability of MgAl-LDH.

3.3 Catalytic mechanism study

3.3.1 Capture of hydroxyl radicals. Coumarin-3-carboxylic acid (C3C) was employed as a probe to detect hydroxyl radicals (˙OH) in the system. As demonstrated by the fluorescence measurements (Fig. 3a), the reaction solution exhibited a significant increase in fluorescence intensity at 450 nm, indicating that C3C effectively trapped ˙OH to form 7-hydroxycoumarin-3-carboxylic acid (7HC3C)[38,39](Fig. S3). The strong fluorescence enhancement confirmed the generation of hydroxyl radicals under the above reaction conditions.

3.3.2 Capture of superoxide anions. Nitroblue tetrazolium (NBT) was used to trap superoxide anions ($O_2^{\bullet-}$) in the reaction system. UV-vis absorption measurements (Fig. 3c) revealed a gradual increase in absorbance at 520 nm as the reaction proceeded, indicating that NBT effectively trapped $O_2^{\bullet-}$ to yield formazan (Fig. S3).[40] The accumulation of this product resulted in enhanced absorbance, confirming the generation of superoxide anions under the above reaction conditions. To exclude

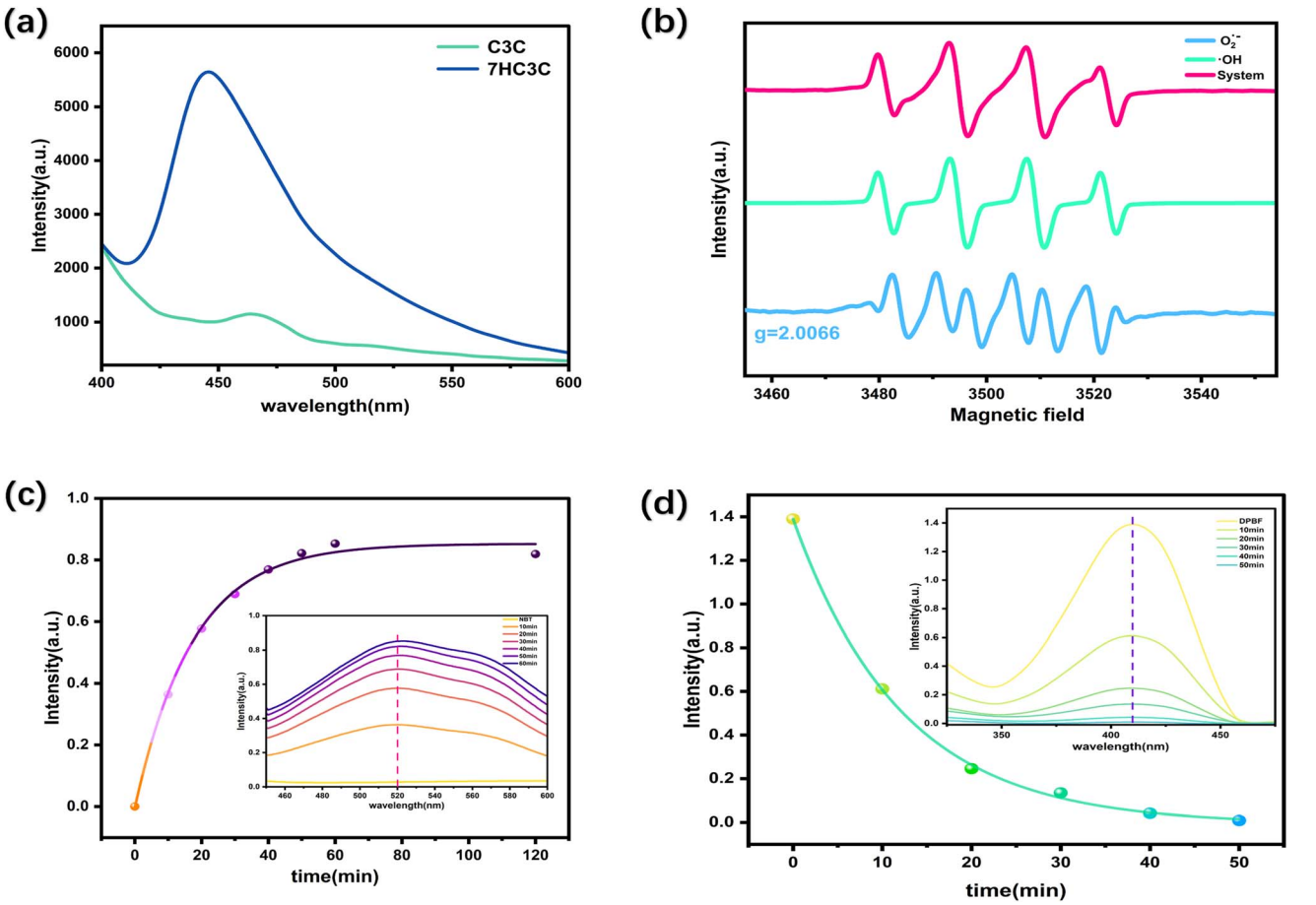

Fig. 3 (a) Fluorescence emission spectra of C3C at the initial stage of the reaction and 7HC3C formed by C3C capturing ˙OH during the reaction. (b) EPR spectra of DMPO ˙OH and $O_2^{\bullet-}$. (c) Time-dependent UV absorption spectra of NBT capturing $O_2^{\bullet-}$ in the reaction solution. (d) Time-dependent UV absorption spectra of DPBF capturing $^1O_2$ in the reaction solution.

the potential interference caused by hydroxyl radicals, electron paramagnetic resonance (EPR) spectroscopy was employed for further analysis. Since DMPO can simultaneously react with both $^{\bullet}OH$ and $O_2^{\bullet-}$, the EPR spectra exhibited a composite signal characteristic of both radical adducts.[41] By fitting the EPR curves, the characteristic splitting pattern of the DMPO–$O_2^{\bullet-}$ adduct was identified (Fig. 3b), providing further evidence for the presence of superoxide anions in the reaction mixture.

3.3.3 Capture of singlet oxygen. 1,3-Diphenylisobenzofuran (DPBF) was employed as a probe to detect singlet oxygen ($^1O_2$) in the system. UV-vis absorption measurements (Fig. 3d) demonstrated a gradual decrease in absorbance at 410 nm as the reaction progressed, indicating that the DPBF effectively trapped $^1O_2$ (Fig. S3).[42–45] The decline in absorbance confirmed the generation of singlet oxygen under the above reaction conditions.

3.3.4 Reaction mechanism and DFT calculations. To identify the products and by-products formed in the reaction, GC-MS analysis was performed. As shown in Fig. S4, in addition to the starting material HTEMP (int1) and the target product HTEMPO (int5), the by-product 2,2,6,6-tetramethylpiperidine-1,4-diol (OHTEMPO, int6) was also detected. To elucidate the roles of various reactive oxygen species (ROS) in the reaction, radical quenching experiments were carried out. The results (Fig. 4b) showed that quenching $O_2^{\bullet-}$ with *p*-benzoquinone (*p*-BQ) led to a sharp decrease in the conversion of HTEMP, indicating that $O_2^{\bullet-}$ have the most significant impact on the reaction. When β-carotene was used in an equivalent amount to quench $^1O_2$, the conversion of HTEMP also decreased, albeit to a lesser extent than with *p*-BQ, suggesting that $^1O_2$ also plays a contributory role in the reaction.[46–49] Moreover, when methanol was used as a quencher for $^{\bullet}OH$,[50] the conversion of HTEMP remained essentially unchanged, while the selectivity slightly increased. This suggested that $^{\bullet}OH$ is primarily responsible for the by-product OHTEMPO. To further investigate the roles of $O_2^{\bullet-}$ and $^1O_2$, a Fenton-like catalyst was constructed using LDHs containing Cu^{2+} and Fe^{3+} ions, which only generated hydroxyl radicals and superoxide anions but not singlet oxygen, as indicated by the results in Table S1.[51] Under these conditions, no significant conversion of HTEMP was observed, indicating that the presence of both $^{\bullet}OH$ and $O_2^{\bullet-}$ alone is insufficient to oxidise HTEMP to HTEMPO. According to relevant literature,[52–54] $^1O_2$ could directly oxidise the int3 (Fig. 4a) formed from the reaction of hindered amines with $^{\bullet}OH$ and $O_2^{\bullet-}$, generating int4 (Fig. 4a). This int4 can further undergo homolytic cleavage with another int3 to form the corresponding hindered amine *N*-oxide. Moreover, hydroxyl radicals, superoxide anions, and singlet oxygen, as common reactive oxygen species, are capable of interconversion under certain conditions.[55–60] Thus, a catalytic mechanism with LDHs as catalysts was proposed (Fig. 4a): LDH acts as a solid base to catalyse the conversion of H_2O_2 into its conjugate base HO_2^- (Fig. S8), which subsequently reacts with another H_2O_2 molecule to generate $^{\bullet}OH$ and $O_2^{\bullet-}$. Through interconversion among the ROS, singlet oxygen is eventually formed. Then, HA reacts with $^{\bullet}OH$ to generate int2, which further reacts with $^{\bullet}OH$ or $O_2^{\bullet-}$ to yield int3. Then int3 reacts with $^1O_2$ or $^{\bullet}OH$ to form int4 or by-product (int6), and int4 subsequently couples with int3 to afford the desired product (int5).

Based on the proposed mechanism, four possible pathways (ac, ad, bc, and bd) were identified for the transformation from intermediate int3 to the final product int5. To further verify the reaction pathway, DFT calculations were performed for each route involved in the reaction mechanism. As shown in Fig. 4c

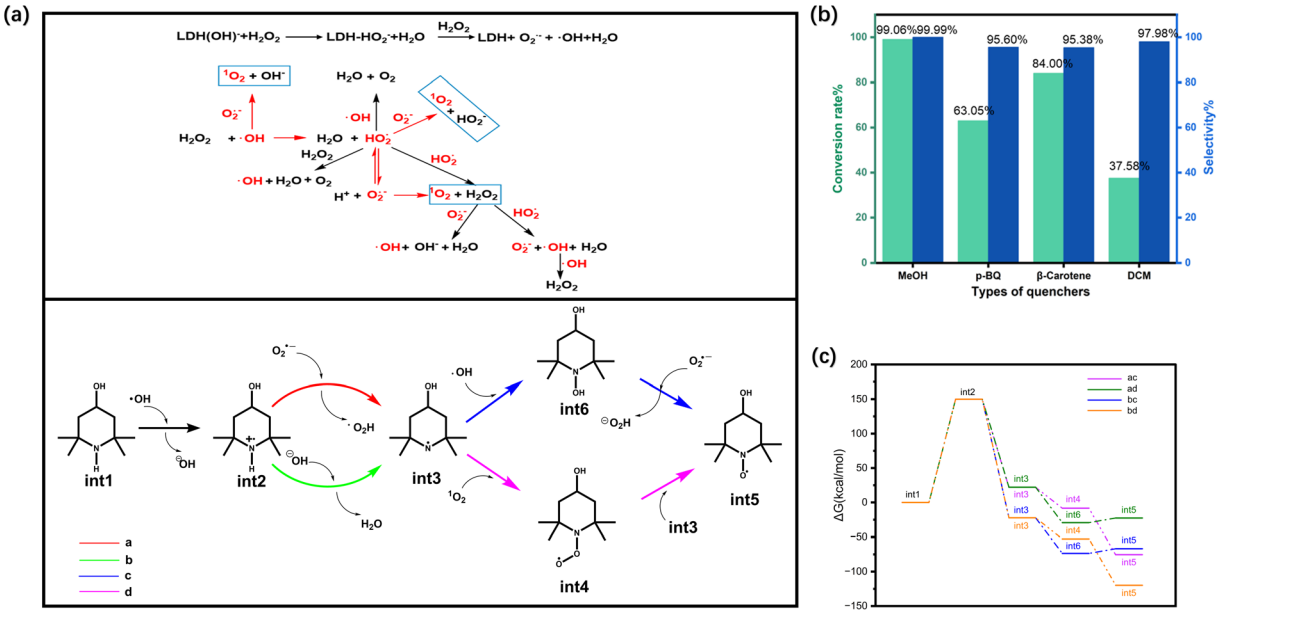

Fig. 4 (a) The interconversion of ROS and the proposed mechanism for the oxidation of hindered amines to nitroxyl radicals. (b) The conversion and selectivity of the reaction in the quenching experiments of ROS. (c) The variation in Δ*G* along different reaction pathways as calculated by DFT.

and Table S5, the theoretical calculation results indicated that for the formation of the target product int5, bc pathway exhibits the largest negative ΔG, suggesting it is the most thermodynamically favourable route. For by-product int6, the ΔG change along bd pathway is the greatest, indicating that this route is more favourable for the formation of by-product int6. Moreover, int6 can be oxidised by the superoxide anion to int5 through a relatively low activation barrier (6.72 kcal mol^{-1}) Theoretical calculations and ROS transformation analysis indicated that $^{\bullet}OH$ primarily oxidise int1 to int3, while $^1O_2$ is mainly responsible for the oxidation of int3 to the target product int5. In parallel, int3 can also be oxidised by $^{\bullet}OH$ to generate by-product int6. Superoxide anion, in addition to serving as essential precursors for $^1O_2$ formation, also contribute to oxidizing part of int6 into int5.[61–65] This mechanistic insight explains why quenching $O_2^{\bullet-}$ leads to a more significant decrease in conversion compared to the quenching of $^1O_2$. According to the proposed mechanism, a higher concentration of singlet oxygen facilitates conversion increasing in the system. The ROS transformation pathways suggest that protic solvents favour the generation of $^1O_2$. To further verify this mechanism, dichloromethane, a non-protic solvent, was employed. The experimental results (Fig. 4b) showed a significant decrease in conversion, providing additional confirmation of the proposed mechanism.

3.4 Investigation on the factors influencing the catalytic performance of the catalyst

According to the above work, hydrotalcite-like catalysts catalyse the decomposition of hydrogen peroxide to generate reactive oxygen species. The key factors influencing their catalytic performance are the type of intercalated anion,[66,67] the extent of surface hydroxyl group exposure, and the strength of the metal ion interaction with surface hydroxide. To identify the primary factors, various hydrotalcite-like systems were further investigated.

3.4.1 Effect of intercalation anions. To assess the effect of interlayer anions, nitrate-intercalated MgAl-LDH was synthesised as a comparison to the carbonate-intercalated MgAl-LDH. XRD characterization (Fig. S5) confirmed the successful synthesis of nitrate-intercalated LDH.[68] The results (Table 1) showed no significant difference in conversion of the reaction, indicating that interlayer anions are not a key factor for this reaction.

3.4.2 Effect of the number of hydroxyl groups exposed on the surface. The number of hydroxyl groups exposed on the LDH lamellae is influenced by both the type of metal ions and their molar ratios. This quantity can be quantitatively compared by analysing the peak areas in CO_2 temperature-programmed desorption (CO_2-TPD) profiles. To investigate the effect of metal ion ratios with the same metal species, MgAl LDHs with Mg/Al molar ratios of 1 : 1 and 4 : 1 were synthesized (Fig. S6). Additionally, MgAl-LDH, NiAl-LDH, ZnAl-LDH, and MgFe-LDH samples exhibiting catalytic activity as shown in Table S1 were selected. These LDHs were sequentially labelled as Mg1Al, Mg4Al, Mg3Al, Ni3Al, Zn3Al, and Mg3Fe. Then, they were subjected to CO_2-TPD test respectively. The results (Fig. 5b and c) showed that at desorption temperatures below 130 °C, corresponding to surface-exposed hydroxyl groups, the peak areas—reflecting hydroxyl quantity—followed the order: Mg3Al > Ni3Al > Mg4Al > Mg3Fe > Mg1Al > Zn3Al. The observed order in the number of exposed hydroxyl groups can be attributed to the influence of the Jahn–Teller effect on the LDH layers. This effect, through lattice stretching and compression, alters the number of surface hydroxyl groups exposed in different LDHs. To confirm that the desorption below 130 °C corresponded to interlayer water instead of dehydration from hydroxyl groups, TGA was conducted for Mg3Al, Ni3Al, Zn3Al, and Mg3Fe (Fig. 5a). The TGA curves confirmed that below 130 °C, only interlayer water was lost, whereas dehydration of hydroxyl groups happened at a higher temperature, validating the accuracy of the CO_2-TPD quantification.

Table 1 Effect of interlayer anions

Anion types	Con.	Sel.
CO_3^{2-}	99.89%	99.29%
NO_3^-	99.56%	95.94%

However, the order of exposed hydroxyl quantity did not correlate with catalytic activity as observed in Table S1. Notably, when using 2.50 wt% Mg4Al for the oxidation of HTEMP, despite having fewer exposed hydroxyl groups than Mg3Al, the conversion efficiency was comparable to that of 5.00wt% Mg3Al (Table S6). These findings indicated that the number of hydroxyl groups exposed on the LDH layers is not the determining factor for their catalytic performance in this system.

3.4.3 The influence of metal ions on the interaction strength with surface hydroxyl groups. For this reaction system, the weaker the interaction between the metal cations and the surface hydroxyl groups, the higher the electron cloud density of the hydroxyl groups, thereby imparting stronger basicity to the metal hydroxides. This enhanced basicity facilitates the catalytic conversion of hydrogen peroxide into its conjugate base (HO_2^-), thus improving the catalytic activity.[69,70] In other words, the stronger the basicity of the LDH, the better its catalytic performance. For LDHs composed of different metal ions, their basicity is primarily determined by the divalent metal cations and can be compared using the pKb values of the corresponding metal hydroxides. According to the optimized conditions shown in Table S1, the catalytic activity of the tested catalysts followed the order: Mg3Al > Zn3Al > Ni3Al, which is consistent with the basicity order of their corresponding hydroxides ($Mg(OH)_2$ > $Zn(OH)_2$ > $Ni(OH)_2$). This further confirmed that the catalytic activity of LDHs is closely related to their basicity.

The basicity of Mg1Al, Mg3Al, and Mg4Al with the same ionic type but different metal ratios can be evaluated by the CO_2 desorption temperatures observed in CO_2-TPD and the binding energy of oxygen in the O 1s spectra obtained from XPS analysis. According to the normalized TPD results (Fig. 5e), the CO_2 desorption temperature followed the order Mg4Al > Mg3Al > Mg1Al, indicating that Mg4Al has the strongest CO_2 adsorption capacity and thus the highest basicity, followed by Mg3Al and

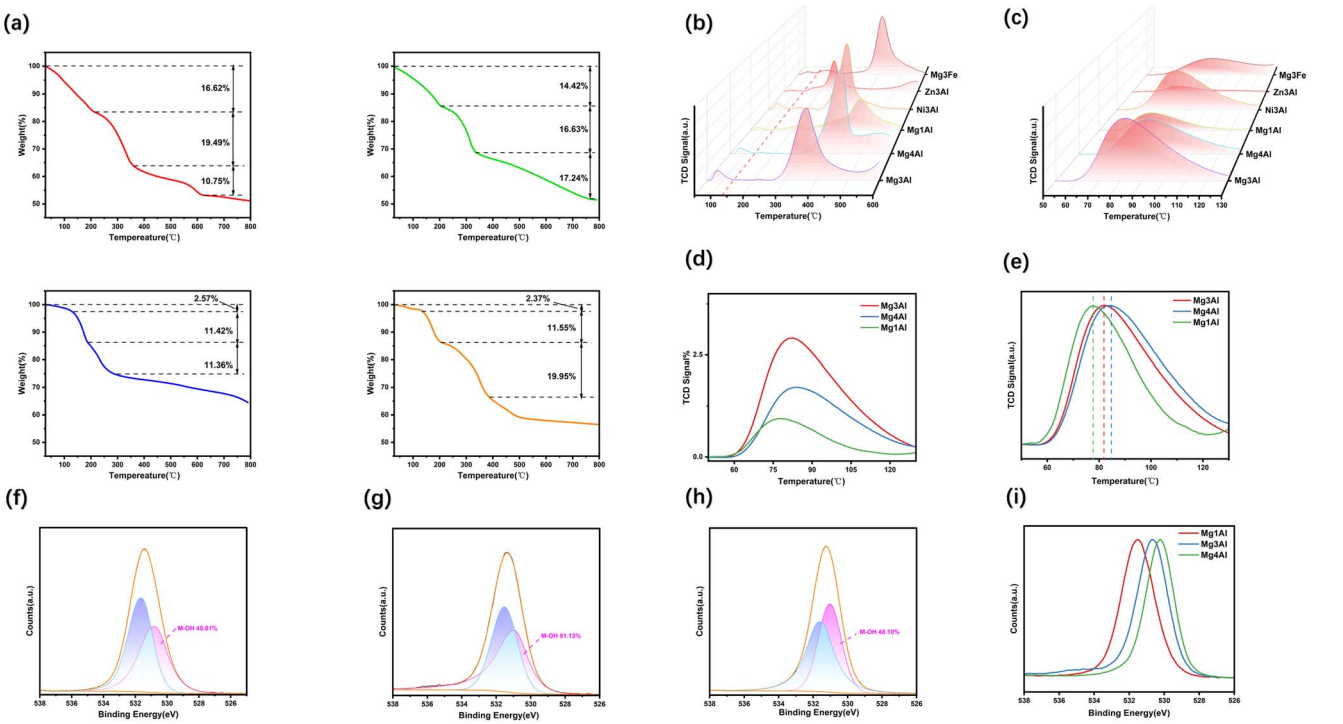

Fig. 5 (a) TG of Mg3Al in red, TG of Ni3Al in green, TG of Zn3Al in blue, and TG of Mg3Fe in brown (b) CO_2-TPD test plot (c) Local zoom in of CO_2-TPD (d) Local zoom in of CO_2-TPD with different Mg–Al ratios (e) Normalised CO_2-TPD with different Mg–Al ratios (f) Split-peak fit of XPS test O 1s for Mg1Al (g) Split-peak fit of XPS test O 1s for Mg3Al (h) Split-peak fit of XPS test O 1s for Mg4Al(i) Normalised XPS test O 1s plot.

Mg1Al with the weakest basicity.[71] Based on the binding energy of O 1s from XPS analysis (Fig. 5i), the O 1s binding energy decreased in the order Mg1Al > Mg3Al > Mg4Al. Since a lower O 1s binding energy corresponds to stronger basicity,[72] this result confirmed the basicity order of Mg4Al > Mg3Al > Mg1Al, which is consistent with the observed superior catalytic performance of Mg4Al. Additionally, deconvolution of the O 1s XPS spectra (Fig. 5f–h) revealed that the surface hydroxyl group content follows the order Mg3Al > Mg4Al > Mg1Al, which agrees with the CO_2-TPD results discussed in Section 3.4.2, further validating the reliability of the characterization.

3.5 Application of the hydrotalcite catalytic system on SEED

To further evaluate the practical potential of this system, a bidentate hindered amine light stabiliser (SEED) was selected for *N*-oxidation to its corresponding nitroxide radical. Using ethanol as the solvent and following the same experimental conditions as described in Section 3.2.1, the SEED conversion reached 99.68% and the product selectivity reached 99.47%. In contrast, the conventional Na_2WO_4 catalytic system yielded a conversion of 97.59% and a selectivity of 92.02%. These results demonstrated that the LDH-H_2O_2 catalytic system offers excellent catalytic performance and can be easily recovered by simple filtration and reused, significantly reducing production cost.

4 Conclusions

LDHs with various metal compositions were synthesized and applied to catalyse the nitroxidation of hindered amines. Among them, the MgAl-LDH with a Mg/Al molar ratio of 3 : 1 demonstrated excellent catalytic performance: with a catalyst loading of 5.00 wt% relative to the substrate, it achieved over 99% conversion of HTEMP and over 99.0% selectivity toward HTEMPO, and could be reused for more than five consecutive cycles. Although the MgAl-LDH with a Mg/Al ratio of 4 : 1 exhibited even higher catalytic activity, its synthesis yield was significantly lower. This reduction in yield is attributed to the aggregation of LDH nanosheets caused by the excessive Mg/Al ratio,[73] a phenomenon directly observable *via* SEM (Fig. S7). Considering both catalytic efficiency and practical feasibility, the Mg/Al = 3 : 1 LDH shows greater potential for real-world application. ROS trapping and quenching experiments, along with the identification of key reaction intermediates, confirmed that the catalytic process involves LDH functioning as a solid base to activate hydrogen peroxide, generating hydroxyl radicals and $O_2^{\bullet-}$. These species can be further converted into $^1O_2$, and the synergistic action of all three ROS leads to the formation of the desired nitroxide radical. TGA, CO_2-TPD, and XPS characterisations revealed that the primary factor influencing the catalytic activity is the type and distribution of metal cations in the LDH catalyst, rather than the interlayer anions or the number of exposed hydroxyl groups. This study expands the catalytic applications of LDHs as solid bases and presents a novel, green, and efficient approach for the *N*-oxidation of hindered amines.

Author contributions

Yupeng Zhang: conceptualization, data curation, investigation, formal analysis and writing – original draft. Wensheng Xu and

Zefan Liu: supervision, resources and validation. Ligong Chen, Xilong Yan, Bowei Wang, and Yang Li: supervision and writing – review & editing.

Conflicts of interest

There are no conflicts to declare.

Data availability

The data supporting this article have been included as part of the supplementary information (SI). Supplementary information is available. See DOI: **https://doi.org/10.1039/d5ra05993c**.

Acknowledgements

We gratefully acknowledge the Large Instrument Management Platform of Tianjin University for providing access to instrumentation and assistance with the measurements.

Notes and references

1 J. Pospíšil and S. Nešpurek, *Prog. Polym. Sci.*, 2000, **25**, 1261–1335.
2 M. Ju, S. Lee, H. M. Marvich and S. Lin, *J. Am. Chem. Soc.*, 2024, **146**, 19696–19703.
3 H. Q. Dai, Y. C. Yuan, L. Dai, X. Sun and L. Wan, *Chinese Pat.*, CN102049248A, 2011.
4 W. Bueschken, M. Kaufhold and P. Bickert, *German Pat.*, DE4219459A1, 1992.
5 M. Kohantorabi, G. Moussavi and S. Giannakis, *Chem. Eng. J.*, 2021, **411**, 127957.
6 X. Zhang, J. Wei, C. Wang, L. Wang, Z. Guo and Y. Song, *Chem. Eng. J.*, 2024, **487**, 150514.
7 Y. Dong, L. Chen, J. Hou, Y. Sun, Z. Han, J. Zhang, Y. Liang, Y. Feng, J. Ren, Q. Li, G. Nie and F. Li, *Nano Today*, 2024, **57**, 102352.
8 T. Hu, Z. Gu, G. R. Williams, M. Strimaite, J. Zha, Z. Zhou, X. Zhang, C. Tan and R. Liang, *Chem. Soc. Rev.*, 2022, **51**, 6126–6176.
9 W. Deng, Q. Tang, S. Huang, L. Zhang, Z. Jia and L. Guo, *Appl. Catal., B*, 2020, **278**, 119336.
10 S. Xia, L. Fang, Y. Meng, X. Zhang, L. Zhang, C. Yang and Z. Ni, *Appl. Catal., B*, 2020, **272**, 118949.
11 M. Devaraj and X. Zhou, *Coord. Chem. Rev.*, 2025, **532**, 216509.
12 H. Wang, W. Zhang, L. Lu, D. Liu, D. Liu, T. Li, S. Yan, S. Zhao and Z. Zou, *Appl. Catal., B*, 2021, **283**, 119639.
13 G. Zhang, X. Zhang, Y. Meng, G. Pan, Z. Ni and S. Xia, *Chem. Eng. J.*, 2020, **392**, 123684.
14 Q. Ye, Z. Huang, P. Wu, J. Wu, J. Ma, C. Liu, S. Yang, S. Rehman, Z. Ahmed, N. Zhu and Z. Dang, *J. Hazard. Mater.*, 2020, **388**, 122120.
15 Z. Jiang, Z. Tang, Y. Hu, H. Shao, G. A. Ayoko and X. Ruan, *Appl. Clay Sci.*, 2025, **276**, 107929.
16 W. Xu, B. Wang, F. Yan, Y. Zeng, S. Liu, W. Fang, L. Chen, X. Yan and Y. Li, *J. Vinyl Addit. Technol.*, 2022, **28**, 530–541.
17 M. Xu and M. Wei, *Adv. Funct. Mater.*, 2018, **28**, 1802943.
18 Z. Chen, X. Wang, Z. Han, S. Zhang, S. Pollastri, Q. Fan, Z. Qu, D. Sarker, C. Scheu, M. Huang and H. Cölfen, *Angew. Chem., Int. Ed.*, 2023, **62**, e202215728.
19 M. J. Frisch, G. W. Trucks, H. B. Schlegel, G. E. Scuseria, M. A. Robb, J. R. Cheeseman, G. Scalmani, V. Barone, G. A. Petersson, H. Nakatsuji, X. Li, M. Caricato, A. V. Marenich, J. Bloino, B. G. Janesko, R. Gomperts, B. Mennucci, H. P. Hratchian, J. V. Ortiz, A. F. Izmaylov, J. L. Sonnenberg, D. Williams-Young, F. Ding, F. Lipparini, F. Egidi, J. Goings, B. Peng, A. Petrone, T. Henderson, D. Ranasinghe, V. G. Zakrzewski, J. Gao, N. Rega, G. Zheng, W. Liang, M. Hada, M. Ehara, K. Toyota, R. Fukuda, J. Hasegawa, M. Ishida, T. Nakajima, Y. Honda, O. Kitao, H. Nakai, T. Vreven, K. Throssell, J. A. Montgomery, J. E. Peralta, F. Ogliaro, M. J. Bearpark, J. J. Heyd, E. N. Brothers, K. N. Kudin, V. N. Staroverov, T. A. Keith, R. Kobayashi, J. Normand, K. Raghavachari, A. P. Rendell, J. C. Burant, S. S. Iyengar, J. Tomasi, M. Cossi, J. M. Millam, M. Klene, C. Adamo, R. Cammi, J. W. Ochterski, R. L. Martin, K. Morokuma, O. Farkas, J. B. Foresman and D. J. Fox, *Gaussian 16, Revision C.01*, Gaussian, Inc., Wallingford, CT, 2016.
20 Y. Zhao and D. G. Truhlar, *Theor. Chem. Acc.*, 2008, **120**, 215–241.
21 F. Weigend and R. Ahlrichs, *Phys. Chem. Chem. Phys.*, 2005, **7**, 3297–3305.
22 D. Kwon, J. Y. Kang, S. An, I. Yang and J. C. Jung, *J. Energy Chem.*, 2020, **46**, 229–236.
23 P. P. Neethu, A. Sreenavya and A. Sakthivel, *Appl. Catal., A*, 2021, **623**, 118292.
24 Z. Zhang, D. Zhou, X. Bao, H. Yu and B. Huang, *Int. J. Hydrogen Energy*, 2018, **43**, 20734–20738.
25 G. Di, Z. Zhu, H. Zhang, J. Zhu, H. Lu, W. Zhang, Y. Qiu, L. Zhu and S. Küppers, *Chem. Eng. J.*, 2017, **328**, 141–151.
26 N. Zhang, B. Zhang, C. Wang, H. Sui, N. Zhang, Z. Wen, A. He, R. Zhang and R. Xue, *J. Colloid Interface Sci.*, 2024, **671**, 110–123.
27 W. J. Kim, M. A. Smeaton, C. Jia, B. H. Goodge, B.-G. Cho, K. Lee, M. Osada, D. Jost, A. V. Ievlev, B. Moritz, L. F. Kourkoutis, T. P. Devereaux and H. Y. Hwang, *Nature*, 2023, **615**, 237–243.
28 B. Xu, G. Pan, X. Fan, H. Zhou, C. Qiu, Y. Guo, M. Xu, J. Sun and X. Xia, *Chem. Eng. J.*, 2025, **503**, 158454.
29 S. Su, X. Li, M. Tan, X. Zhang, Y. Wang, Y. Duan, J. Peng and M. Luo, *Inorg. Chem. Front.*, 2023, **10**, 869–879.
30 Z. Karami, M. Jouyandeh, J. A. Ali, M. R. Ganjali, M. Aghazadeh, S. M. R. Paran, G. Naderi, D. Puglia and M. R. Saeb, *Prog. Org. Coat.*, 2019, **136**, 105218.
31 Z. Karami, M. Jouyandeh, S. Ghiyasi, J. A. Ali, M. R. Ganjali, M. Aghazadeh, M. Maadani, M. Rallini, F. Luzi, L. Torre, D. Puglia and M. R. Saeb, *Prog. Org. Coat.*, 2020, **139**, 105255.
32 T. Sudare, M. Dubois, N. Louvain, M. Kiyama, F. Hayashi and K. Teshima, *Inorg. Chem.*, 2020, **59**, 1602–1610.
33 H. Zhang, K. Li, Z. Liang, Y. Wan, Z. Feng, J. Liu, Q. Zhang and M. Wang, *J. Phys. Chem. Solids*, 2022, **170**, 110932.

34 R. kumar Allada, A. Navrotsky, H. T. Berbeco and W. H. Casey, *Science*, 2002, **296**, 721–723.
35 L. Zhao, X. Li, C. Hao and C. L. Raston, *Appl. Catal., B*, 2012, **117–118**, 339–345.
36 J. R. Goldstein and A. C. C. Tseung, *J. Catal.*, 1974, **32**, 452–465.
37 M. L. Kremer, *J. Catal.*, 1962, **1**, 351–355.
38 A. C. Maier, E. H. Iglebaek and M. Jonsson, *ChemCatChem*, 2019, **11**, 5435–5438.
39 S. J. De-Nasri, S. Nagarajan, P. K. J. Robertson and V. V. Ranade, *Chem. Eng. J.*, 2021, **420**, 127560.
40 G. Matula and P. Y. Paterson, *N. Engl. J. Med.*, 1971, **285**, 311–317.
41 R. Lo Scalzo, *Eur. Food Res. Technol.*, 2021, **247**, 2253–2265.
42 Z.-H. Xie, C.-S. He, D.-N. Pei, Y. Dong, S.-R. Yang, Z. Xiong, P. Zhou, Z.-C. Pan, G. Yao and B. Lai, *Chem. Eng. J.*, 2023, **468**, 143778.
43 P. R. Ogilby, *Chem. Soc. Rev.*, 2010, **39**, 3181–3209.
44 T. Entradas, S. Waldron and M. Volk, *J. Photochem. Photobiol., B*, 2020, **204**, 111787.
45 X. Chen, F. Wang, J. Y. Hyun, T. Wei, J. Qiang, X. Ren, I. Shin and J. Yoon, *Chem. Soc. Rev.*, 2016, **45**, 2976–3016.
46 Y. Guo, J. Long, J. Huang, G. Yu and Y. Wang, *Water Res.*, 2022, **215**, 118275.
47 C. Sun, Y. Wang, B. Jiang, S. Hu, Y. Wang, C. Zhang, F. Liu, Y. Zhang and G. Li, *Chem. Eng. J.*, 2023, **477**, 146942.
48 G. S. Beddard, R. S. Davidson and K. R. Trethewey, *Nature*, 1977, **267**, 373–374.
49 M. Garavelli, F. Bernardi, M. Olivucci and M. A. Robb, *J. Am. Chem. Soc.*, 1998, **120**, 10210–10222.
50 B. Li, B. Chen and Z. Wei, *J. Hazard. Mater.*, 2024, **478**, 135502.
51 A. G. Parts, *Nature*, 1951, **168**, 79.
52 J. R. Roberts and K. U. Ingold, *J. Am. Chem. Soc.*, 1973, **95**, 3228–3235.
53 G. Nardi, I. Manet, S. Monti, M. A. Miranda and V. Lhiaubet-Vallet, *Free Radicals Biol. Med.*, 2014, **77**, 64–70.
54 L. Chen, S. Yamane, J. Mizukado, Y. Suzuki, S. Kutsuna, T. Uchimaru and H. Suda, *Chem. Phys. Lett.*, 2015, **624**, 87–92.
55 X. Li, X. Li, C. Wang and B. Wang, *J. Colloid Interface Sci.*, 2023, **648**, 778–786.
56 H.-W. Lee, J. Hwang, J.-Y. Kim, G. N. Morais, K. S. Tang, M. Choi, H. Choi, H.-B. Youn, S.-T. Kim, J. H. Ha, S. J. Kang, S. Chen, S.-E. Suh and W.-J. Kwak, *Adv. Mater.*, 2025, **37**, 2415805.
57 Y. Nosaka and A. Y. Nosaka, *Chem. Rev.*, 2017, **117**, 11302–11336.
58 Y. Guo, G. Yu, U. von Gunten and Y. Wang, *Water Res.*, 2023, **242**, 120158.
59 Y. Peng, Z. Bian, F. Wang, S. Li, S. Xu and H. Wang, *J. Hazard. Mater.*, 2024, **462**, 132797.
60 H. Sun, N. Jiang, G. Yu and J. Li, *Chem. Eng. J.*, 2023, **475**, 146014.
61 P. Wang, L. Wang, R. Xiao, S. Qiu, J. Cao, Y. Fu and Z. Wang, *Chem. Eng. J.*, 2025, **505**, 159531.
62 B. G. Kwon, *J. Photochem. Photobiol., A*, 2008, **199**, 112–118.
63 N. Serpone, Y. M. Artemev, V. K. Ryabchuk, A. V. Emeline and S. Horikoshi, *Curr. Opin. Green Sustainable Chem.*, 2017, **6**, 18–33.
64 E. Dobbelaar, C. Rauber, T. Bonck, H. Kelm, M. Schmitz, M. E. de Waal Malefijt, J. E. M. N. Klein and H.-J. Krüger, *J. Am. Chem. Soc.*, 2021, **143**, 13145–13155.
65 M. Lovisari and A. R. McDonald, *Inorg. Chem.*, 2020, **59**, 3659–3665.
66 W. Hu, L. Chen, B. Geng, Y. Song, Z. Wu, Q. Zheng, G. Shan and M. Du, *Chem. Eng. J.*, 2023, **468**, 143694.
67 B. M. Hunter, W. Hieringer, J. R. Winkler, H. B. Gray and A. M. Müller, *Energy Environ. Sci.*, 2016, **9**, 1734–1743.
68 Y. Cao, S. Fang, K. Chen, H. Qi, X. Zhang, C. Huang, J. Wang and J. Liu, *Appl. Sci.*, 2022, **12**, 4492.
69 W. Bing, L. Zheng, S. He, D. Rao, M. Xu, L. Zheng, B. Wang, Y. Wang and M. Wei, *ACS Catal.*, 2018, **8**, 656–664.
70 Q. Liu, C. Wang, W. Qu, B. Wang, Z. Tian, H. Ma and R. Xu, *Catal. Today*, 2014, **234**, 161–166.
71 O. Klepel and B. Hunger, *J. Therm. Anal. Calorim.*, 2005, **80**, 201–206.
72 F. M. P. R. van Laar, D. E. De Vos, F. Pierard, A. Kirsch-De Mesmaeker, L. Fiermans and P. A. Jacobs, *J. Catal.*, 2001, **197**, 139–150.
73 J.-Y. Lee, G.-H. Gwak, H.-M. Kim, T. Kim, G. J. Lee and J.-M. Oh, *Appl. Clay Sci.*, 2016, **134**, 44–49.